IEEE Access
Multidisciplinary | Rapid Review | Open Access Journal

Received July 22, 2019, accepted August 21, 2019, date of publication August 28, 2019, date of current version September 13, 2019.

Digital Object Identifier 10.1109/ACCESS.2019.2937978

Fractional-Order PID Motion Control for AUV Using Cloud-Model-Based Quantum Genetic Algorithm

JUNHE WAN[1], BO HE[1], (Member, IEEE), DIANRUI WANG[1], TIANHONG YAN[2], AND YUE SHEN[1]

[1]School of Information Science and Engineering, Ocean University of China, Qingdao 266100, China
[2]School of Mechanical Electrical Engineering, China Jiliang University, Hangzhou 310018, China

Corresponding author: Yue Shen (shenyue@ouc.edu.cn)

This work was supported in part by the Natural Key Research and Development Program of China under Grant 2016YFC0301400, and in part by the Natural Science Foundation of China under Grant 51379198.

ABSTRACT Aiming to improve the performance of motion for autonomous underwater vehicle (AUV), a fractional-order PID strategy is proposed. It is a more generalized form for the conventional integer-order PID controller, keeping its simplicity and utilizing the generalized derivative and integral control actions. The fractional-order PID controller has been successfully applied to heading control, diving control and path-following system of AUV on sea trial. In addition, the fractional-order closed-loop system has proven to be stable. By comparing simulations and experiments, the satisfactory performance, such as overshoot, settling time and steady-state error, has been achieved. The cloud-model-based quantum genetic algorithm (CQGA) is employed to tune coefficients of fractional-order PID controller. The quantum bits and quantum superposition states avoid the pressure of selection and maintain the diversity of population in chromosome coding. Due to the randomness and stability tendency of cloud droplets, the cloud crossover operator and the cloud mutation operator can effectively overcome the shortcomings of premature and slow searching speed. Numerical simulations show that the CQGA is more efficient to find the optimal coefficients of fractional-order PID controller than GA.

INDEX TERMS Fractional-order PID, AUV, cloud-model-based quantum genetic algorithm (CQGA), steady error.

I. INTRODUCTION

AUV has been an active field of research and development in exploring unknown marine environment and carrying out different military missions. Motion control systems for AUV have become very challenging due to strong coupling, high nonlinearity and external disturbances. A variety of control systems are available, such as PID control [1], [2], sliding mode control [3], [4], H_∞ control [5], [6] and adaptive control [7]. Nevertheless, the PID (proportional integral derivative) control is still the most widely used in AUV because of the simplicity and reliability. The fractional-order PID [8], [9] is a more generalized form for the conventional integer-order PID controller, keeping the simplicity of PID and utilizing the generalized derivative and integral control actions. The fractional-order PID controller was introduced by Podlubny [10], [11], namely the $PI^\lambda D^\mu$ controller, where λ and μ are the orders of the integrator and differentiator, respectively.

Nowadays, the application of fractional-order PID controller in AUV is still at primary stage. Joshi S D et al. designed a fractional-order PID controller for depth and steering system of AUV. Its simulation results showed that the fractional-order PID was superior to traditional PID with respect to overshoot and settling time [12]–[14]. Ajmal et al. dealt with the development of tuning a fractional-order PID controller by loop shaping approach for controlling the depth of an AUV. Through the comparison between the simulation results it was clear that the fractional-order PID controller can be well implemented on integer-order depth system. The rise time, settling time, and overshoot are well improved than integer-order PID [15]. Radmehr et.al proposed an improved fractional-order PID controller for the control of AUV motion with

The associate editor coordinating the review of this article and approving it for publication was Sara Dadras.

six degrees of freedom (DOF). Genetic algorithm (GA) was employed to find suboptimal coefficients of fractional-order PID controller [16]. Nevertheless, these applications have been performed in theory simulation, and little research has been conducted to examine on sea trial. In this paper, the fractional-order PID controller will be utilized on AUV platform.

It is essential to study tuning methods of five parameters (K_p, K_d, K_i, λ, μ). There are many optimization methods for fractional-order PID controller such as genetic algorithms(GA) [16], [17], particle swarm optimization(PSO) [18], [19] and gravitational search algorithm [20]. Here we will concentrate our attention on cloud-model-based quantum genetic algorithm(CQGA) [22].

As a novel optimization algorithm, CQGA combines cloud-model theory with quantum genetic algorithm(QGA). QGA is based on the concept and principles of quantum computing, such as a quantum bit and superposition of states [23], [24]. It uses a Q-bit as a probabilistic representation, which is defined as the smallest unit of information. Meanwhile, quantum rotation gate is used as the update mechanism, which could help guide the searching direction to the optimal area and maintain the diversity of population [25]. The cloud-model theory [26], [27] is introduced based on QGA. The cloud crossover operator and cloud mutation operator are generated by cloud generator [28]. As a consequence of the randomness and stability tendency of cloud drops, the algorithm will overcome the shortcomings of premature and lower searching ability.

The remainder of this paper is organized as follows. In Section II, a dynamic model of AUV is established and simulations are conducted. The controller design, parameters optimization and the proof of stability of fractional-order closed-loop system are explained in Section III. A set of comparisons are carried out by simulations and experiments in Section IV, and the results are also being discussed. Finally, Section V summarizes the key conclusions of this work.

II. VEHICLE MODEL

A. ESTABLISHING COORDINATE SYSTEM

The notation, term and coordinate system are defined by SNAME (Society of Naval Architects and Marine Engineers) and ITTC (International Towing Tank Conference). The world-fixed coordinate system (E-$\xi\eta\zeta$) has its origin E fixed to the earth [29]. The body-fixed coordinate system ($o-xyz$) with origin O is a moving reference frame that is fixed to AUV (see Fig.1).

For AUV, the motion components of six degrees of freedom are easily defined as surge (u), sway (v), heave (w), roll (p), pitch (q) and yaw (r). $U = [u, v, w, p, q, r]^T$ is the linear and angular velocities with respect to the body-fixed reference frame, and $\tau = [X, Y, Z, K, M, N]^T$ is a vector of forces and moments acting on AUV with respect to the body-fixed reference frame. The Euler angles are heading angle ψ, pitch angle θ and roll angle ϕ. $P^W = [\xi, \eta, \zeta]$ is a position vector with respect to the world-fixed reference frame,

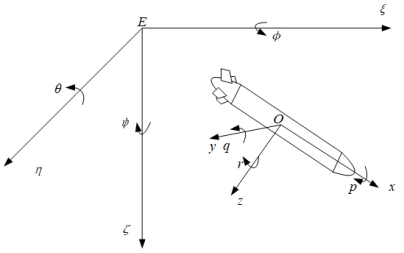

FIGURE 1. Coordinate system of AUV. {*Body*}: ($x, y, z, u, v, w, p, q, r$), {*World*} : ($\xi, \eta, \zeta, \phi, \theta, \psi$).

TABLE 1. Notions used for AUV.

Vector	X-axis	Y-axis	Z-axis
Linear velocity	u	v	ω
Angular velocity	p	q	r
Euler Angle	ϕ	θ	ψ
Force	X	Y	Z
Moment	K	M	N

and $P^B = [x, y, z]$ is a position vector with respect to the body-fixed reference frame [30].The notations are summarized in Table 1. The transformation between the body-fixed and world-fixed position is given by (1).

$$\begin{bmatrix} \xi \\ \eta \\ \zeta \end{bmatrix} = T \begin{bmatrix} x \\ y \\ z \end{bmatrix} \tag{1}$$

$$T = \begin{bmatrix} c\psi c\theta & c\psi s\theta s\phi - s\psi c\phi & s\psi s\theta s\phi + c\psi c\phi \\ s\psi c\theta & s\psi s\theta s\phi + c\psi c\phi & s\psi s\theta c\phi - c\psi s\phi \\ -s\theta & c\theta s\phi & c\theta c\phi \end{bmatrix} \tag{2}$$

where T is rotation matrix, $c(\cdot)$ denotes $cos(\cdot)$ and $s(\cdot)$ denotes $sin(\cdot)$. The inverse transformation is obtained as (3).

$$\begin{bmatrix} x \\ y \\ z \end{bmatrix} = T^{-1} \begin{bmatrix} \xi \\ \eta \\ \zeta \end{bmatrix} \tag{3}$$

$$T^{-1} = \begin{bmatrix} c\psi c\theta & s\psi c\phi & -s\theta \\ c\psi s\theta s\phi - s\psi c\phi & s\psi s\theta s\phi + c\psi c\phi & c\theta s\phi \\ c\psi s\theta c\phi + s\psi s\phi & s\psi s\theta s\phi - c\psi c\phi & c\theta c\phi \end{bmatrix} \tag{4}$$

where T^{-1} is inverse matrix of T.

B. DYNAMIC MODEL OF AUV

It is well known that the spatial motion of AUV in six degrees of freedom is strongly coupled and highly non-linear. To simplify AUV modeling for further analysis, it is assumed that the port-starboard (xz-plane) is symmetric. In general, the force of AUV can be separated into two types: one is the hydrodynamic force F_{vis} (or resistance force) with respected to an AUV moving in fluid, the other is the external force F_{else}, such as the rudder force, propulsion force, gravity and buoyancy, etc. The equation can be written as (5) [31].

$$E\dot{U} = F_{vis} + F_{else} \tag{5}$$

where E is defined as (6), as shown at the top of the next page, considering xz plane of symmetry. where m: AUV mass;
x_G, y_G, z_G: position of center of gravity for AUV;
x_B, y_B, z_B: position of center of buoyancy for AUV;

$$E = \begin{bmatrix} m - X_{\dot{u}} & 0 & 0 & 0 & mz_G & 0 \\ 0 & m - Y_{\dot{v}} & 0 & -mz_G - Y_{\dot{p}} & 0 & -Y_{\dot{r}} \\ 0 & 0 & m - Z_{\dot{w}} & 0 & -Z_{\dot{q}} & 0 \\ 0 & -mz_G - Y_{\dot{p}} & 0 & I_x - K_{\dot{p}} & 0 & -K_{\dot{r}} \\ mz_G & 0 & -Z_{\dot{q}} & 0 & I_y - M_{\dot{q}} & 0 \\ 0 & -Y_{\dot{r}} & 0 & -K_{\dot{r}} & 0 & I_z - N_{\dot{r}} \end{bmatrix} \tag{6}$$

I_x, I_y, I_z: moments of inertia about x, y and z axes;
$X_{\dot{u}}$, $Y_{\dot{v}}$, $Y_{\dot{r}}$, $Z_{\dot{w}}$, $Z_{\dot{q}}$, $K_{\dot{p}}$, $K_{\dot{r}}$, $M_{\dot{q}}$, $N_{\dot{v}}$, $N_{\dot{r}}$: hydrodynamic coefficients;
$U = [u, v, w, p, q, r]^T$: velocity (angular velocity) of six degrees of freedom;
$\dot{U} = [\dot{u}, \dot{v}, \dot{w}, \dot{p}, \dot{q}, \dot{r}]^T$: acceleration (angular acceleration) of six degrees of freedom;
$F_{vis} = [X_{vis}, Y_{vis}, Z_{vis}, K_{vis}, M_{vis}, N_{vis}]^T$: hydrodynamic forces and moments.

$$\begin{cases} X_{vis} = m(vr - wq) + \frac{1}{2}\rho L^4[X'_{qq}q^2 + X'_{rr}r^2 + X'_{rp}rp] \\ \quad +\frac{1}{2}\rho L^3[X'_{vr}vr + X'_{wq}wq] \\ \quad +\frac{1}{2}\rho L^2[X'_{uu}u^2 + X'_{vv}v^2 + X'_{ww}w^2] \\ Y_{vis} = m(wp - vr) + \frac{1}{2}\rho L^4[Y'_{pq}pq + Y'_{qr}qr] \\ \quad +\frac{1}{2}\rho L^3[Y'_{vq}vq + Y'_{wp}wp + Y'_{wr}wr] \\ \quad +\frac{1}{2}\rho L^3[Y'_{r}ur + Y'_{p}up + Y'_{v|r|}\frac{v}{|v|}|(v^2 + w^2)^{\frac{1}{2}}||r|] \\ \quad +\frac{1}{2}\rho L^2[Y'_{0}u^2 + Y'_{v}uv + Y'_{v|v|}|(v^2 + w^2)^{\frac{1}{2}}|] \\ \quad +Y'_{vw}vw \\ Z_{vis} = m(uq - vp) + \frac{1}{2}\rho L^4[Z'_{pp}p^2 + Z'_{rr}r^2 + Z'_{rp}rp] \\ \quad +\frac{1}{2}\rho L^3[Z'_{vr}vr + Z'_{vp}vp] \\ \quad +\frac{1}{2}\rho L^3[Z'_{q}uq + Z'_{w|q|}\frac{w}{|w|}|(v^2 + w^2)^{\frac{1}{2}}||q|] \\ \quad +\frac{1}{2}\rho L^2[Z'_{0}u^2 + Z'_{w}uw + Z'_{w|w|}w|(v^2 + w^2)^{\frac{1}{2}}|] \\ \quad +\frac{1}{2}\rho L^2[Z'_{|w|}u|w| + Z'_{ww}|w(v^2 + w^2)^{\frac{1}{2}}|] \\ \quad +\frac{1}{2}\rho L^2 Z'_{vv}v^2 \\ K_{vis} = mz_G(vr - wp) + \frac{1}{2}\rho L^5[K'_{qr}qr + K'_{pq}pq \\ \quad +K'_{p|p|}p|p|] + \frac{1}{2}\rho L^4[K'_{p}up + K'_{r}ur] \\ \quad +\frac{1}{2}\rho L^4[K'_{vq}vq + K'_{wp}wp + K'_{wr}wr] \\ \quad +\frac{1}{2}\rho L^3[K'_{0}u^2 + K'_{v}uv + K'_{v|v|}v|(v^2 + w^2)^{\frac{1}{2}}|] \\ \quad +\frac{1}{2}\rho L^3 K'_{vw}vw \\ M_{vis} = mz_G(vr - wq) + \frac{1}{2}\rho L^5[M'_{pp}p^2 + M'_{rr}r^2 + M'_{rp}rp \\ \quad +M'_{q|q|}q|q|] + \frac{1}{2}\rho L^4[M'_{vr}vr + M'_{vp}vp] \\ \quad +\frac{1}{2}\rho L^4[M'_{q}uq + M'_{|w|q}|(v^2 + w^2)^{\frac{1}{2}}q] \\ \quad +\frac{1}{2}\rho L^3[M'_{0}u^2 + M'_{w}uw + M'_{w|w|}w|(v^2 + w^2)^{\frac{1}{2}}|] \\ \quad +\frac{1}{2}\rho L^3[M'_{|w|}u|w| + M'_{ww}|w(v^2 + w^2)^{\frac{1}{2}}|] \\ \quad +\frac{1}{2}\rho L^3 M'_{vv}v^2 + (I_z - I_x)pr \\ N_{vis} = \frac{1}{2}\rho L^5[N'_{pq}pq + N'_{qr}qr + N'_{r|r|}r|r|] \\ \quad +\frac{1}{2}\rho L^4[N'_{wr}wr + N'_{wp}wp + N'_{vq}vq] \\ \quad +\frac{1}{2}\rho L^4[N'_{p}up + N'_{r}ur + N'_{|v|r}|(v^2 + w^2)^{\frac{1}{2}}r] \\ \quad +\frac{1}{2}\rho L^4[N'_{0}u^2 + N'_{v}uv + N'_{v|v|}v|(v^2 + w^2)^{\frac{1}{2}}|] \\ \quad +\frac{1}{2}\rho L^3 N'_{vw}vw + (I_x - I_y)pq \end{cases} \tag{7}$$

The auxiliary equation of motion is depicted as (8).

$$\begin{cases} \dot{\phi} = p + \dot{\psi}s\theta \\ \dot{\theta} = qc\phi - rs\phi \\ \dot{\psi} = \dfrac{rc\phi - qs\phi}{c\theta} \\ \dot{\xi} = uc\theta c\psi + v(s\phi s\theta c\psi - c\psi s\psi) \\ \quad +w(s\phi s\psi - c\phi s\theta c\psi) \\ \dot{\eta} = uc\theta s\psi + v(c\phi c\psi - s\phi s\theta s\psi) \\ \quad +w(c\phi s\theta s\psi - s\phi c\psi) \\ \dot{\zeta} = -us\theta + vc\theta s\phi + wc\theta c\phi \end{cases} \tag{8}$$

The sea is approximately homogeneous mixed layer in the area of 0-100 meters. The influence of temperature, salinity and density of sea water on the motion of AUV can be neglected, therefore only the ocean current should be taken into account [32]. The ocean current is assumed to be a constant in time, uniform in space, and irrotational with respect to the world-fixed coordinate system. The speed of AUV influenced by ocean current is depicted in (9).

$$\begin{cases} u_r = u - U_c c\theta c(\alpha_c - \psi) \\ v_r = v - U_c s\theta \\ w_r = w - U_c s\theta c(\alpha_c - \psi) \end{cases} \tag{9}$$

where U_c is the ocean current velocity of an irrotational fluid, and α_c is the angle of ocean current. After the time derivative, (9) can be written in component form as (10).

$$\begin{cases} \dot{u}_r = \dot{u} + U_c qs\theta c(\alpha_c - \psi) - U_c rc\theta s(\alpha_c - \psi) \\ \dot{v}_r = \dot{v} - U_c s(\alpha_c - \psi) \\ \dot{w}_r = \dot{w} + U_c qc\theta c(\alpha_c - \psi) - U_c rs\theta s(\alpha_c - \psi) \end{cases} \tag{10}$$

Hence, the relative velocity and acceleration vectors U and $\dot{U}$ are described in (11) and (12) respectively.

$$U = [u + u_r, v + v_r, w + w_r, p, q, r] \tag{11}$$

$$\dot{U} = [\dot{u} + \dot{u}_r, \dot{v} + \dot{v}_r, \dot{w} + \dot{w}_r, \dot{p}, \dot{q}, \dot{r}] \tag{12}$$

C. GRAVITY

Let m be the mass of AUV, ∇ the volume displaced by AUV, g the acceleration of gravity and ρ the seawater density. Obviously, the weight and buoyancy are expressed

as $W = mg$, $B = \rho g \nabla$ respectively.

$$G = \begin{bmatrix} -(W-B)s\theta \\ (W-B)c\theta s\phi \\ (W-B)c\theta c\phi \\ (y_G - y_B)Wc\theta c\phi - (z_G - z_B)Wc\phi s\phi \\ -(x_G - x_B)Wc\theta c\phi - (z_G - z_B)Ws\theta \\ (x_G - x_B)Wc\theta s\phi - (y_G - y_B)Ws\theta \end{bmatrix} \tag{13}$$

For neutrally buoyant vehicles $W = B$, therefore (13) simplifies to (14).

$$G = \begin{bmatrix} 0 \\ 0 \\ 0 \\ (y_G - y_B)Wc\theta c\phi - (z_G - z_B)Wc\phi s\phi \\ -(x_G - x_B)Wc\theta c\phi - (z_G - z_B)Ws\theta \\ (x_G - x_B)Wc\theta s\phi - (y_G - y_B)Ws\theta \end{bmatrix} \tag{14}$$

An even simpler representation is obtained as shown in (15), on account of $x_G = x_B$, $y_G = y_B$ and $h = z_G - z_B$.

$$G = \begin{bmatrix} 0 & 0 & 0 & -hWc\phi s\phi & -hWs\theta & 0 \end{bmatrix}^T \tag{15}$$

D. EQUATION OF MOTION IN THE HORIZONTAL PLANE

In order to analyze manipulating motion, the equation of motion can be divided into two noninteracting subsystems, the horizontal subsystem and the vertical subsystem. The following assumptions will be applied to the dynamic model: the AUV only moves at a low speed and the center of gravity is in the origin of the body-fixed coordinate system. Neglecting the elements corresponding to heave, roll and pitch, the horizontal equation of motion is generalized in (16).

$$\begin{cases} m(\dot{u} - vr) = X \\ m(\dot{v} + ur) = Y \\ I_z \dot{r} = N \end{cases} \tag{16}$$

The X equation can be eliminated due to the fact that cruise speed u is a constant and $\dot{u}$ is zero. The fore and aft of AUV are asymmetrical, therefore the linearized maneuvering equation can be written in (17).

$$\begin{cases} (m - Y_{\dot{v}})\dot{v} - Y_v v + Y_{\dot{r}}\dot{r} + (mu - Y_r)r = Y_{\delta_r}\delta_r \\ (I_z - N_{\dot{r}})\dot{r} - N_r r + N_{\dot{v}}\dot{v} - N_v v = N_{\delta_r}\delta_r \end{cases} \tag{17}$$

As a result of starboard-port symmetry of AUV, $Y_{\dot{r}}$ and $N_{\dot{v}}$ are zero. Equation (17) simplifies to (18).

$$\begin{cases} (m - Y_{\dot{v}})\dot{v} - Y_v v + (mu - Y_r)r = Y_{\delta_r}\delta_r \\ (I_z - N_{\dot{r}})\dot{r} - N_r r - N_v v = N_{\delta_r}\delta_r \end{cases} \tag{18}$$

where δ_r is the rudder angle. Eliminating v and ignoring the element corresponding to roll finally yields (19). A_1, A_0, B_2, B_1 and B_0 are presented in (20) and (21), respectively.

$$B_2\ddot{r} + B_1\dot{r} + B_0 r = A_1\dot{\delta}_r + A_0\delta_r \tag{19}$$

$$\begin{cases} A_1 = (m - Y_{\dot{v}})N_{\delta_r} \\ A_0 = Y_{\delta_r}N_v - N_{\delta_r}Y_v \end{cases} \tag{20}$$

$$\begin{cases} B_2 = (I_z - N_{\dot{r}})(m - Y_{\dot{v}}) \\ B_1 = -Y_v(I_z - N_{\dot{r}}) - N_r(m - Y_{\dot{v}}) \\ B_0 = N_v(mV - Y_r) + Y_v N_r \end{cases} \tag{21}$$

Hence, applications of Laplace's transformation are presented in (22) and (23)($\dot{\psi} = r$).

$$G_1(s) = \frac{r}{\delta_r}(s) = \frac{A_1 s + A_0}{B_2 s^2 + B_1 s + B_0} \tag{22}$$

$$G_2(s) = \frac{\psi}{\delta_r}(s) = \frac{A_1 s + A_0}{B_2 s^3 + B_1 s^2 + B_1 s} \tag{23}$$

Substituting the hydrodynamic coefficients into (23), the transfer function becomes (24).

$$G_2(s) = \frac{1.9s + 2.8}{s^3 + 4.5s^2 + 4.4s} \tag{24}$$

E. EQUATION OF MOTION IN THE VERTICAL PLANE

Neglecting the elements corresponding to sway, roll and yaw, the vertical equation of motion is generalized in (25).

$$\begin{cases} m\dot{u} = X \\ m(\dot{w} + u_0 q) = Z \\ I_y \dot{q} = M \end{cases} \tag{25}$$

The X equation can be eliminated due to the fact that cruise speed u is a constant and $\dot{u}$ is zero. The top and bottom of AUV are asymmetrical, therefore the linearized maneuvering equation can be written in (26).

$$\begin{cases} (m - Z_{\dot{w}})\dot{w} - Z_w w + Z_{\dot{q}}\dot{q} + (mu + Z_q)q = Z_0 + Z_{\delta_s}\delta_s \\ (I_y - M_{\dot{q}})\dot{q} - M_q q - M_{\dot{w}}\dot{w} - M_w w = M_0 + M_{\delta_s}\delta_s + M_\theta\theta \end{cases} \tag{26}$$

As a consequence of starboard-port symmetry of AUV, $Z_{\dot{q}}$ and $M_{\dot{w}}$ are zero. Equation (26) simplifies to (27).

$$\begin{cases} (m - Z_{\dot{w}})\dot{w} - Z_w w + (mu + Z_q)q = Z_0 + Z_{\delta_s}\delta_s \\ (I_y - M_{\dot{q}})\dot{q} - M_q q - M_w w = M_0 + M_{\delta_s}\delta_s + M_\theta\theta \end{cases} \tag{27}$$

where $M_\theta\theta$ is the righting moment, ($\dot{\theta} = q$); δ_s is the stern plane angle.

Eliminating $w, \dot{w}, q, \dot{q}$ and ignoring the element corresponding to roll finally yields (28). C_1, C_0, D_3, D_2, D_1 and D_0 are presented in (29) and (30), respectively.

$$D_3\dddot{\theta} + D_2\ddot{\theta} + D_1\dot{\theta} + D_0 = C_1\dot{\delta}_s + C_0\delta_s \tag{28}$$

$$\begin{cases} C_1 = (m - Z_{\dot{w}})M_{\delta_s} \\ C_0 = (Z_{\delta_s}M_w - Z_w M_{\delta_s})M_w \end{cases} \tag{29}$$

$$\begin{cases} D_3 = (I_y - M_{\dot{q}})(m - Z_{\dot{w}}) \\ D_2 = -M_{\dot{q}}(m - Z_{\dot{w}}) - (I_y - M_{\dot{q}})Z_w \\ D_1 = M_q Z_w - M_\theta(m - Z_{\dot{w}}) - M_w(mu + Z_q) \\ D_0 = M_\theta Z_w \end{cases} \tag{30}$$

Hence, applications of Laplace's transformation are presented in (31).

$$G_3(s) = \frac{\theta}{\delta_s}(s) = \frac{C_1 s + C_0}{D_3 s^3 + D_2 s + D_1 s + D_0} \tag{31}$$

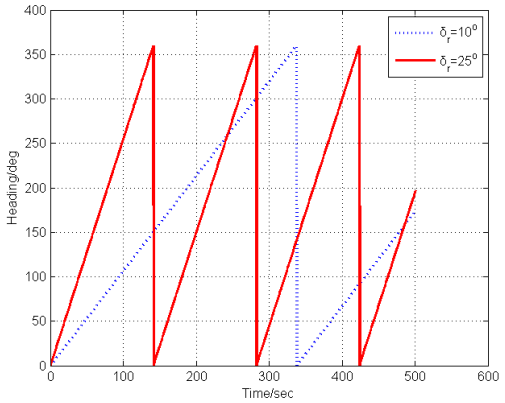

FIGURE 2. Comparison of heading angle with different rudders. The red solid line denotes $\delta_r = 10°$; the blue dots denote $\delta_r = 25°$ ($\delta_s = 0°$).

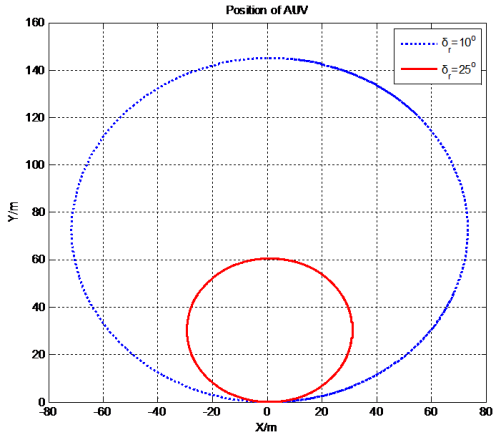

FIGURE 3. Comparison of position with different rudders. The red solid line denotes $\delta_r = 10°$; the blue dots denote $\delta_r = 25°$ ($\delta_s = 0°$).

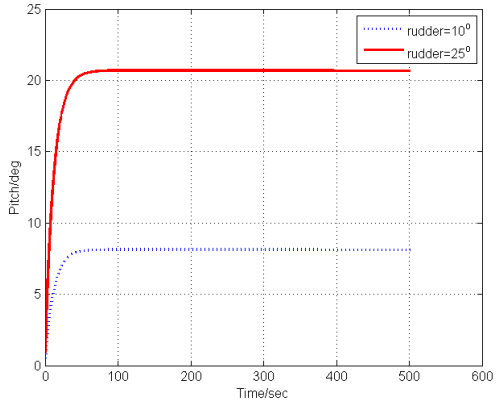

FIGURE 4. Comparison of pitch angle with different stern rudders. The red solid line denotes $\delta_s = 10°$; the blue dots denote $\delta_s = 25°$ ($\delta_r = 0°$).

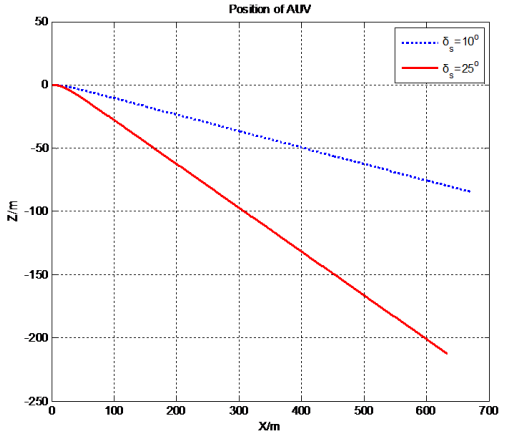

FIGURE 5. Comparison of position with different stern rudders. The red solid line denotes $\delta_s = 10°$; the blue dots denote $\delta_s = 25°$ ($\delta_r = 0°$).

Substituting the hydrodynamic coefficients into (31), the transfer function becomes (32).

$$G_3(s) = \frac{1.6s + 1.8}{s^3 + 4.5s^2 + 6s + 0.5} \tag{32}$$

F. SIMULATOINS

It is assumed that the sea is sufficiently large to sail and the AUV can withstand significant amounts of stress.

1) SIMULATIONS IN THE HORIZONTAL PLANE

The stern rudder is kept to zero. The rotational motion is performed and AUV's trajectory is a circle in the horizontal plane, as shown in Fig.2 and Fig.3. The rudder angles are 10° and 25° for 500s respectively. The turning radius is 30m corresponding to the rudder angle 25°, while the turning radius is 73m corresponding to the rudder angle 10°. The red solid line is over twice the cycle number of the blue dots. It is significant that the smaller the rudder angle, the bigger the turning radius is.

2) SIMULATIONS IN THE VERTICAL PLANE

The rudder angle is kept to zero. The diving motion is performed and AUV's trajectory is a straight line in the vertical plane, as shown in Fig.4 and Fig.5. The stern rudder angles are 10° and 25° for 500s respectively. The pitch angle is 8° corresponding to the stern rudder angle 10°, while the pitch angle is 21° corresponding to the stern rudder angle 25°. The depth is approximately 85m and 210m respectively. The red solid line is over twice the depth of the blue dots. It is significant that the bigger the stern rudder angle, the bigger the pitch and the depth are.

3) SIMULATIONS IN THE THREE-DIMENSIONAL SPACE

The rudder angle and the stern rudder angle are kept to 10° and 25° for 1000s respectively, as shown in Fig.6 and Fig.7. The diving and rotational motions are performed and AUV's trajectory is a spiral line in the three-dimensional space. The stern rudder angles and rudder angles are 10° and 25°, respectively. The red dashed line is over twice the cycle number of the blue line. The bigger the rudder is, the faster the AUV dives.

III. CONTROLLER DESIGN

A. FUNDAMENTALS OF FRACTIONAL-ORDER CALCULUS

The inspiration of fractional calculus has taken birth since 300 years ago. Leibniz and L'Hôpital first discussed the

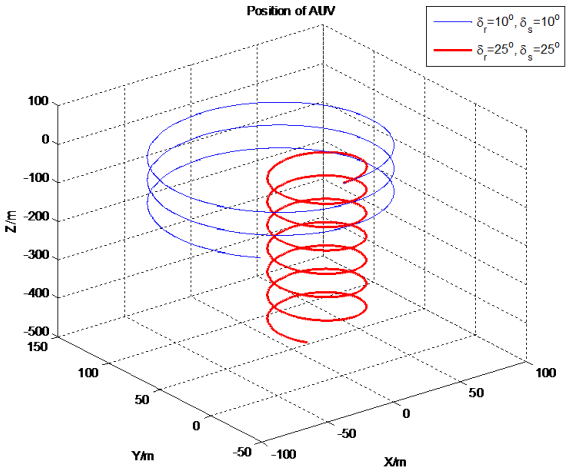

FIGURE 6. Comparison of position with different rudders and stern rudders in the three-dimensional space. (The blue line indicates $\delta_r = 10°$, $\delta_s = 10°$; the red dashed line indicates $\delta_r = 25°$, $\delta_s = 25°$).

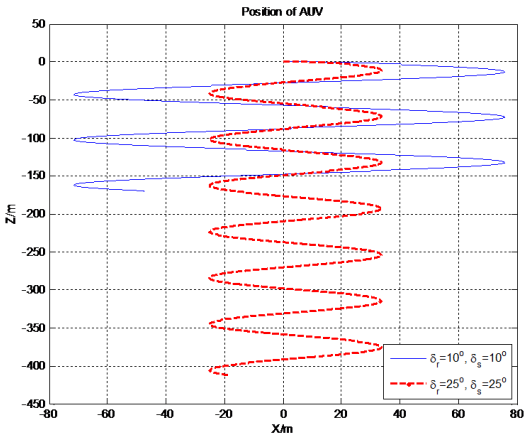

FIGURE 7. Comparison of position with different rudders and stern rudders in the vertical plane. (The blue line indicates $\delta_r = 10°$, $\delta_s = 10°$; the red dashed line indicates $\delta_r = 25°$, $\delta_s = 25°$).

TABLE 2. Parameters matric with different rudders.

Angle	Turning radius(m)	Depth(m)	Cycle number
$\delta_r = 10°, \delta_s = 10°$	73	170	2.5
$\delta_r = 25°, \delta_s = 25°$	25	410	6.5

fractional derivative in 1695 by giving half-order derivative. The most commonly used for fractional order calculus definitions are given by Grünwald-Letnikov, Cauchy, Riemann-Liouville, and Caputo.

Grünwald-Letnikov's definition can be expressed as (33).

$$ {}_a^{GL}\mathscr{D}_t^{\alpha} f(t) = \lim_{h\to 0} h^{-\alpha} \sum_{i=0}^{[\frac{t-a}{h}]} (-1)^i \binom{a}{i} f(t-ih) \tag{33} $$

Cauchy's definition can be expressed as (34).

$$ {}_a\mathscr{D}^{\alpha} f(t) = \frac{\alpha(\alpha+1)}{2\pi j} \oint_C \frac{f(\tau)}{(\tau - t)^{\alpha+1}} d(\tau) \tag{34} $$

Riemann-Liouville's definition can be expressed as (35).

$$ {}_a^{RL}\mathscr{D}_t^{-\alpha} f(t) = \frac{1}{\Gamma(\alpha)} \int_a^t (t-\tau)^{(\alpha-1)} f(\tau) d(\tau) \tag{35} $$

Caputo's definition can be expressed as (36).

$$ {}_a\mathscr{D}_t^{\alpha} f(t) = \frac{1}{\Gamma(1-\alpha)} \int_0^t \frac{f(\tau)}{(t-\tau)^{\alpha}} d(\tau) \tag{36} $$

where $\Gamma(\cdot)$ is the *Gamma* function as in (37) and α represents the fractional order, $\alpha \in (0, 1)$.

$$ \Gamma(z) = \int_0^{\infty} e^{-t} t^{z-1} dt \tag{37} $$

B. FRACTIONAL-ORDER PID CONTROLLER

A fractional-order PID controller is described in time domain as (38).

$$ u(t) = K_p e(t) + K_i \mathscr{D}^{-\lambda} e(t) + K_d \mathscr{D}^{\mu} e(t) \tag{38} $$

The frequency domain description of fractional-order PID controller is given by (39).

$$ C(s) = K_p + K_i s^{-\lambda} + K_d s^{\mu} \tag{39} $$

where K_p is the proportional gain, K_i the integral gain and K_d the differential gain, λ and μ are the order of integral and differential controller, such that $\lambda, \mu \in (0, 1)$ respectively.

Taking $\lambda = 1$ and $\mu = 1$, it is obtained a conventional PID controller. $\lambda = 1$ and $\mu = 0$ give a PI controller, $\lambda = 0$ and $\mu = 1$ give a PD controller. It is apparent that all these controllers are particular cases of fractional-order PID controller. In a graphical way, the fractional-order PID controller is depicted in Fig. 8, extending the four control points of the conventional PID to the range of the quarter-plane. The fractional-order PID controller for AUV is designed in Fig.9.

The transfer function of fractional-order closed-loop system of heading is illustrated as (40). The parameters of fractional-order PID controller for heading is presented in Table 4.

$$ G_{sh}(s) = \frac{G_2(s)C(s)}{1 + G_2(s)C(s)} = \frac{P_{sh}(s)}{Q_{sh}(s)} \tag{40} $$

$P_{sh}(s) = (A_1 s + A_0)(K_p + K_i s^{-\lambda} + K_d s^{\mu})$;

$Q_{sh}(s) = s(B_2 s^2 + B_1 s + B_0) + (A_1 s + A_0)(K_p + K_i s^{-\lambda} + K_d s^{\mu})$.

The transfer function of fractional-order closed-loop system of pitch is illustrated as (41). The parameters of fractional-order PID controller for pitch is presented in Table 4.

$$ G_{sp}(s) = \frac{G_3(s)C(s)}{1 + G_3(s)C(s)} = \frac{P_{sp}(s)}{Q_{sp}(s)} \tag{41} $$

$P_{sp}(s) = (C_1 s + C_0)(K_p + K_i s^{-\lambda} + K_d s^{\mu})$;

$Q_{sp}(s) = (D_3 s^3 + D_2 s^2 + D_1 s + D_0) + (C_1 s + C_0)(K_p + K_i s^{-\lambda} + K_d s^{\mu})$.

An appropriate approximation technique, *Oustaloup* recursive filter, is proposed in [38]. It gives a very good

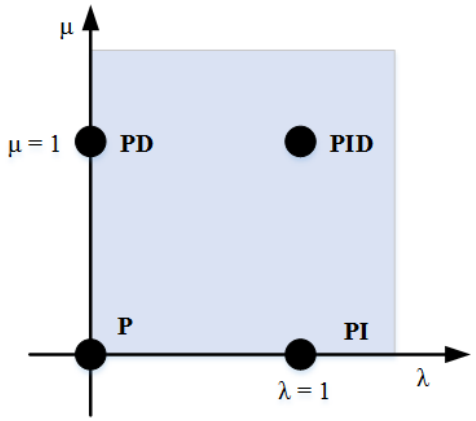

FIGURE 8. Fractional-order PID controller plane.

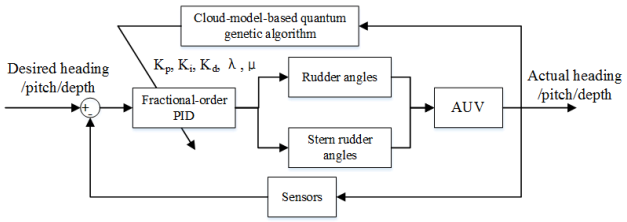

FIGURE 9. The structure of FOPID controller for AUV

approximation of a fractional differentiator of order α and a fractional integrator of order $-\alpha$ using (42)-(44). N is the order of approximation in the valid frequency range. The *Oustaloup* filter is employed for simulation in the frequency range of $\omega = [\omega_b, \omega_h] = [0.001, 1000]\ rad/s$ and the order of approximation is $N = 5$.

$$s^{\alpha} \approx K \prod_{k=1}^{N} \frac{s + w'_k}{s + w_k} \tag{42}$$

$$w'_k = w_b \cdot w_u^{(2k-1-\alpha)/N}, \quad w_k = w_b \cdot w_u^{(2k-1+\alpha)/N} \tag{43}$$

$$w_u = \sqrt{w_b/w_h}, K = w_h^{\alpha} \tag{44}$$

C. NUMERICAL SOLUTIONS

The Grünwald-Letnikov's definition is extremely advantageous to obtain a numerical solution, as shown in (45). The recursive formula (46) is utilized to compute the coefficients with a fixed value of derivative and integral order α. The *short memory principle* was proposed for the numerical solution of fractional-order PID controller.

$${}_0\mathscr{D}_t^{\alpha} f(t) \approx {}_{t-L}\mathscr{D}_t^{\alpha} f(t) \approx h^{-\alpha} \sum_{i=0}^{N(t)} \omega_i^{\alpha} f(t - ih) \tag{45}$$

$$\omega_i^{\alpha} = (-1)^i \binom{a}{i} \tag{46}$$

$$\omega_0^{\alpha} = 1; \omega_i^{\alpha} = (1 - \frac{\alpha + 1}{i})\omega_{i-1}^{\alpha} (i = 1, 2, \cdots .) \tag{47}$$

where L is the memory length, h is the step size of calculation, $[x]$ represents the integer part of x, and $N(t) = \min\{[\frac{t}{h}], [\frac{L}{h}]\} = \min\{m, [\frac{L}{h}]\}$.

Considering the computational efficiency, the memory length L is reasonably determined in a permitted range of accuracy. Substituting (45) into (38), the numerical solution of fractional-order PID controller is illustrated as (48).

$$u(m) = K_p e(m) + K_i h^{\lambda} \sum_{i=0}^{N(t)} \omega_i^{\alpha} e(m-i) + K_d h^{-\mu} \sum_{i=0}^{N(t)} \omega_i^{\alpha} e(m-i) \tag{48}$$

D. STABILITY

In the integer-order system, it is well known from the theory of stability that all the roots of $Q(s) = 0$ have negative real parts. It means that they are located on the left half of the complex plane. The stability of fractional-order system differs from the integer case. It is interesting that a stable fractional system may have roots in the right half of complex plane. The stable region of fractional-order system is given by Fig.10.

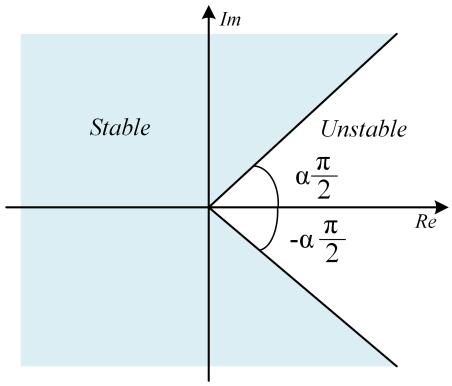

FIGURE 10. Stable region of fractional-order systems with order $0 < \alpha < 1$.

Theorem 1 (Matignon, 1998) [33]: A commensurate-order system described by a rational transfer function (53) is stable if and only if the following condition is satisfied (54).

$$G(\gamma) = \frac{P(\gamma)}{Q(\gamma)} \tag{53}$$

$$|arg(\gamma_i)| > \alpha \frac{\pi}{2} \tag{54}$$

where $\gamma = s^{\alpha}$ and γ_i is the i-th root of $Q(\gamma)$.

The transfer function of closed-loop fractional-order system of heading is depicted in (49), as shown at the bottom of the next page. The characteristic equation of commensurate-order system is a polynomial of the complex variable $\gamma = s^{\alpha}$, where α is assigned to 0.01, as shown in (50), as shown at the bottom of the next page. All the poles of γ equation is illustrated in Fig.11(left), and the enlargement of stable region boundary is given in Fig.11(right). The absolute value of the argument minimum 0.0306 *rad* is larger than $\alpha\pi/2 = 0.0157\ rad$.

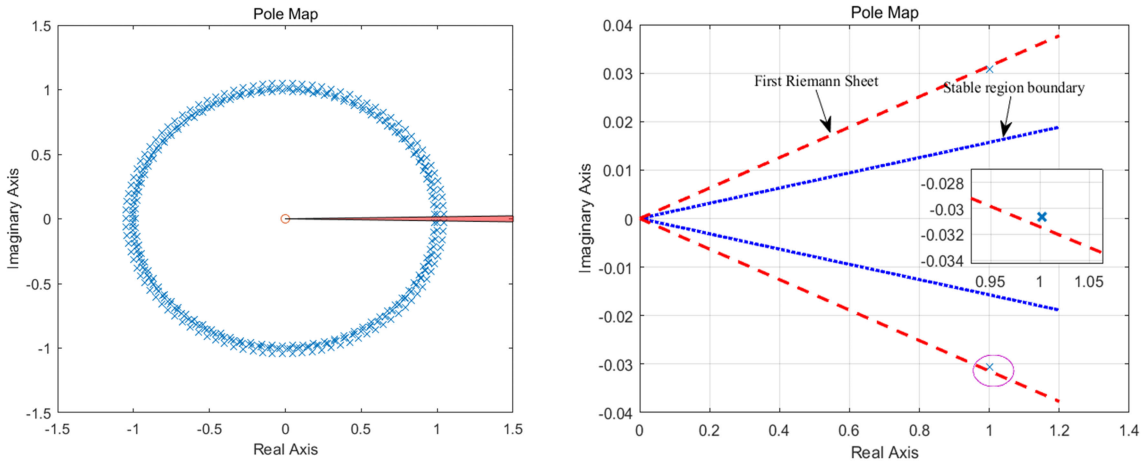

FIGURE 11. Stability analysis of fractional-order heading systems with commensurate-order $\alpha = 0.01$, Pole positions(left), Enlargement(right).

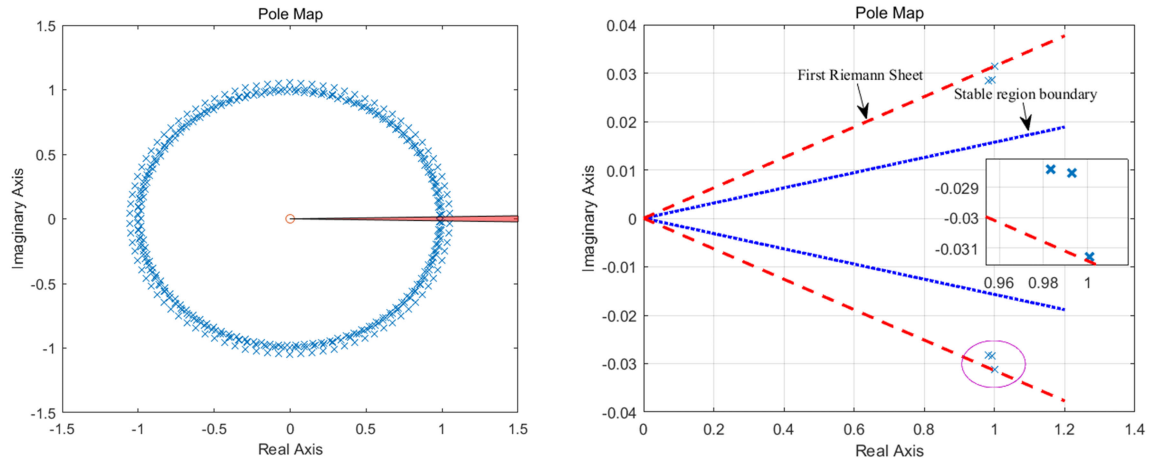

FIGURE 12. Stability analysis of fractional-order pitch systems with commensurate-order $\alpha = 0.01$, Pole positions(left), Enlargement(right).

The pair of complex conjugate roots $(1.002 \pm 0.0307i)$ are located between the first Riemann sheet and stable region boundary. The roots of γ convert into s, and they both have the negative real parts $(-1.2770 \pm 0.1066i)$. Therefore, **Theorem 1** is satisfied and the closed-loop fractional-order system of heading is stable.

The transfer function of closed-loop fractional-order system of pitch is described as (51), as shown at the bottom of the this page. The characteristic equation is shown in (52), as shown at the bottom of the this page. The poles of γ equation are illustrated in Fig.12(left), and the enlargement of stable region boundary is given in Fig.12(right).

$$G_{sh}(s) = \frac{112.1s^{2.88} + 180.5s^{1.89} + 165.2s^{1.88} + 49.4s + 266s^{0.89} + 72.8}{s^{3.89} + 4.5s^{2.89} + 112.1s^{2.88} + 184.9s^{1.89} + 165.2s^{1.88} + 49.4s + 266s^{0.89} + 72.8} \tag{49}$$

$$G_{sh}(s) = \frac{112.1\gamma^{288} + 180.5\gamma^{189} + 165.2\gamma^{188} + 49.4\gamma^{100} + 266\gamma^{89} + 72.8}{\gamma^{389} + 4.5\gamma^{289} + 112.1\gamma^{288} + 184.9\gamma^{189} + 165.2\gamma^{188} + 49.4\gamma^{100} + 266\gamma^{89} + 72.8} \tag{50}$$

$$G_{sp}(s) = \frac{94.4s^{3.09} + 106.2s^{2.19} + 64s^{2.09} + 72s^{1.09} + 8s + 9}{s^{4.09} + 94.4s^{3.19} + 4.5s^{3.09} + 106.2s^{2.19} + 70s^{2.09} + 72.5s^{1.09} + 8s + 9} \tag{51}$$

$$G_{sp}(s) = \frac{94.4\gamma^{309} + 106.2\gamma^{219} + 64\gamma^{209} + 72\gamma^{109} + 8\gamma^{100} + 9}{\gamma^{409} + 94.4\gamma^{319} + 4.5\gamma^{309} + 106.2\gamma^{219} + 70\gamma^{209} + 72.5\gamma^{109} + 8\gamma^{100} + 9} \tag{52}$$

The absolute value of the argument minimum 0.0287 *rad* is larger than $\alpha\pi/2 = 0.0157$ *rad*. There are three pairs of poles between the first Riemann sheet and stable region boundary ($1.0009 \pm 0.0313i$, $0.9929 \pm 0.0285i$, $0.9832 \pm 0.0284i$). The roots of γ convert into s, and they all have the negative real parts ($-1.1542 \pm 0.0183i$, $-0.4932 \pm 0.1364i$, $-0.1869 \pm 0.0485i$). Obviously, all the poles of the closed-loop system are located in the stable region. Therefore, **Theorem 1** is satisfied and the closed-loop fractional-order system of pitch is stable.

E. PARAMETERS OPTIMIZATION USING CLOUD-MODEL-BASED QUANTUM GENETIC ALGORITHM

The fractional-order PID controller gives better performance owing to extra two parameters introduced than conventional PID. Tuning these five parameters has become an important research subject in control systems. The cloud-model-based quantum genetic algorithm (CQGA) is employed to optimize the parameters of fractional-order PID controller.

1) QUANTUM GENETIC ALGORITHM

The smallest unit of information stored in a two state quantum computer is called a quantum bit or qubit. A qubit may be in the "1" state, in the "0" state, or in any linear superposition of the two. The state of a qubit can be represented as (55).

$$|\varphi\rangle = \alpha|0\rangle + \beta|1\rangle \tag{55}$$

where α and β are complex numbers that specify the probability amplitudes of the corresponding states. $|\alpha|^2$ gives the probability that the qubit will be found in the "0" state and $|\beta|^2$ gives the probability that the qubit will be found in the "1" state. Normalization of the state to unity guarantees as (56).

$$|\alpha|^2 + |\beta|^2 = 1 \tag{56}$$

A Q-bit individual as a string of m Q-bits is defined as (57).

$$G = \begin{vmatrix} \alpha_1 & \alpha_2 & \cdots & \alpha_m \\ \beta_1 & \beta_2 & \cdots & \beta_m \end{vmatrix} \tag{57}$$

where $|\alpha_i|^2 + |\beta_i|^2 = 1$, $i = 1, 2, \cdots, m$. This representation has a quite superiority that one Q-bit individual can represent 2^m states at the same time. For instance, there is a three-Q-bits system. The state of system can be represented as (58). However, at least eight states (000), (001), (010), (011), (100), (101), (110) and (111) are required in binary representation. QGA can explore the search space with a smaller number of individuals and exploit the search space for a global solution within a short span of time.

$$\begin{aligned}|\varphi\rangle = {} & a_{000}|000\rangle + a_{001}|001\rangle + a_{010}|010\rangle + a_{011}|011\rangle \\ & + a_{100}|100\rangle + a_{101}|101\rangle + a_{110}|110\rangle + a_{111}|111\rangle \end{aligned} \tag{58}$$

$$\begin{aligned}& |a_{000}|^2 + |a_{001}|^2 + |a_{010}|^2 + |a_{011}|^2 \\ & + |a_{100}|^2 + |a_{101}|^2 + |a_{110}|^2 + |a_{111}|^2 = 1 \end{aligned} \tag{59}$$

There are several quantum gates, such as the Not gate, controlled NOT gate, rotation gate, Hadamard gate, etc, which are selected according to the practical conditions. The rotation gate is applied to generate the probability amplitude of quantum states which is an important updating method in quantum genetic algorithm. The quantum rotation door for fractional-order PID optimization problem can be chosen in order to maintain diversity of population.

$$U(\vartheta_i) = \begin{bmatrix} cos(\vartheta_i) & -sin(\vartheta_i) \\ sin(\vartheta_i & cos(\vartheta_i) \end{bmatrix} \tag{60}$$

where $U(\vartheta_i)$ is a unitary matrix, ϑ_i is a rotation angle.

The unitary matrix of rotation gate is employed to update a Q-bit individual as a variation operator, the process is as (61).

$$\begin{vmatrix} \alpha_i' \\ \beta_i' \end{vmatrix} = U(\vartheta_i) \begin{vmatrix} \alpha_i \\ \beta_i \end{vmatrix} = \begin{bmatrix} cos(\vartheta_i) & -sin(\vartheta_i) \\ sin(\vartheta_i & cos(\vartheta_i) \end{bmatrix} \begin{vmatrix} \alpha_i \\ \beta_i \end{vmatrix} \tag{61}$$

2) CLOUD MODEL

The cloud model acts as a converted model between a qualitative concept and its quantitative expression. It has three numerical characteristics: E_x, E_n, and H_e, as shown in Fig.13.

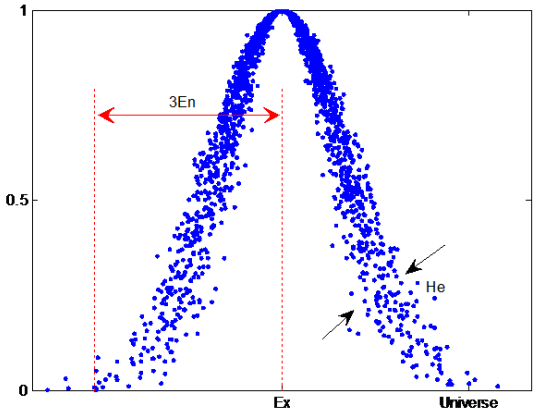

FIGURE 13. Cloud model.

The expectation E_x is the position corresponding to the center of the cloud gravity. The entropy E_n is the uncertainty measurement of the qualitative concept, which is determined by both the randomness and the fuzziness of the concept. It reflects the bandwidth of the mathematical expectation curve of the normal cloud and represents the value region in which the drop is accepted to the linguistic term. H_e is the uncertainty measurement of the entropy-that is, the entropy of the entropy-which is a measure of the dispersion on the cloud drops [34](see Algorithm 1).

3) CLOUD-MODEL-BASED QUANTUM GENETIC ALGORITHM

The cloud model is introduced based on the QGA taking advantage of randomness and stability tendency of cloud drops. The cloud crossover operator and cloud mutation

Algorithm 1 Forward Normal Cloud Generator

Input: (E_x, E_n, H_e), n (the number of cloud drops);
Output: $Drop(x_i, \mu_i), i = 1, 2, \ldots, n$; n of cloud drops x and their certainty degree μ;
Steps:
(1) $E_n' = \text{RANDN}(E_n, H_e)$; Generate a normally distributed random number E_n' with expectation E_n and variance H_e;
(2) $x_i = \text{RANDN}(E_n, E_n')$; Generate a normally distributed random number x_i' with expectation E_x and variance E_n';
(3)Evaluate $\mu_i = e^{\frac{-(f-E_x)^2}{2E_n'^2}}$
(4)$Drop(x_i, \mu_i)$; x_i with certainty degree of μ_i is a cloud drop
(5) Repeat steps (1)-(4) until n cloud drops are generated.

operator are described as (62) and (63), which are generated by cloud generator with respect to the fitness value of functions (see Algorithm 2).

$$p_c = \begin{cases} t_1 e^{\frac{-(f-E_x)^2}{2E_n'^2}} & f \geq \bar{F} \\ t_2 & f < \bar{F} \end{cases} \tag{62}$$

$$p_m = \begin{cases} s_1 e^{\frac{-(f-E_x)^2}{2E_n'^2}} & f \geq \bar{F} \\ s_2 & f < \bar{F} \end{cases} \tag{63}$$

where $\bar{F}$ represents the average fitness value of the population;
f denotes the larger of the fitness values of the solutions to be crossed;
t_1, t_2, s_1, s_2 are the constants.

Algorithm 2 Cloud-Model-Based Quantum Genetic Algorithm

Initialization: the size of initial population, sampling time, iterative generation, etc. $\alpha_i = \frac{1}{\sqrt{2}}, \beta_i = \frac{1}{\sqrt{2}}$ Generate the initial population randomly;
(1)Evaluate the fitness value of each individual as the target of next evolution values
(2)record the best scheduling results;
(3)Determine the iteration termination conditions: if met, terminate the algorithm, else go on;
(4)Execute the cloud crossover operator p_c;
(5)Execute the cloud mutation operator p_m;
(6)Update using rotation quantum gate;
(7)Generate t = t + 1 and algorithm return to step (3).

Due to the randomness and stability tendency of cloud droplets, the quantum genetic algorithm can be effectively improved to overcome the shortcomings of premature and slow searching speed by the cloud crossover operator and the cloud mutation operator.

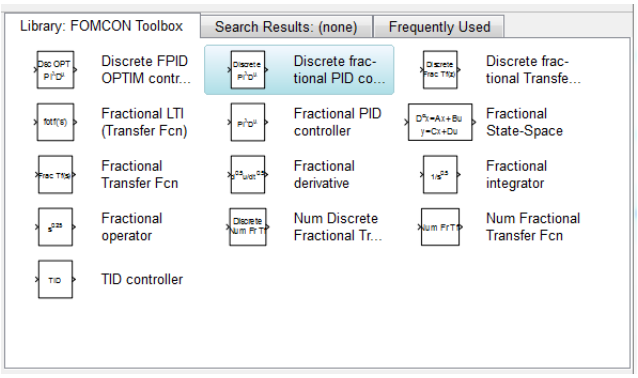

FIGURE 14. FOMCON Simulink library.

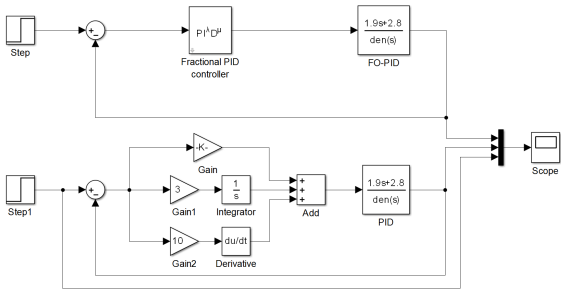

FIGURE 15. Simulink model of heading angle for AUV using FOPID and PID controllers.

IV. EXPERIMENT RESULTS AND ANALYSIS

A. SIMULATIONS

In this paper, FOMCON toolbox is employed for simulations. FOMCON (Fractional order Modeling and Control) is a new MATLAB toolbox, which offers a set of tools for researchers in the field of fractional-order control [35]–[37]. The Simulink modeling library currently provided is showcased in Fig.14. The blocks of fractional-order PID controller are utilized for heading, pitch and diving system analysis.

1) HEADING ANGLE

Figure 15 illustrates the Simulink model of heading angle using fractional-order PID and PID controllers. The comparisons of step response are shown in Fig.16. It is clear that the fractional-order PID controller has lower settling time and overshoot. The disturbance of ocean current is simulated by white noise as shown in Fig.17. It is further proved the availability of fractional-order PID controller.

2) PITCH ANGLE

Figure 18 illustrates the Simulink model of pitch angle using fractional-order PID and PID controllers. The comparisons of step response in two different scenarios are depicted in Fig.19 and Fig.20. There is no overshoot in the first scenario. They are with the same rise time in the second scenario. The results is reported in Table 7. It is clear that the fractional-order PID controller has lower settling time without overshoot, whereas it has smaller overshoot with the same settling time. The disturbance of ocean current is simulated by white noise

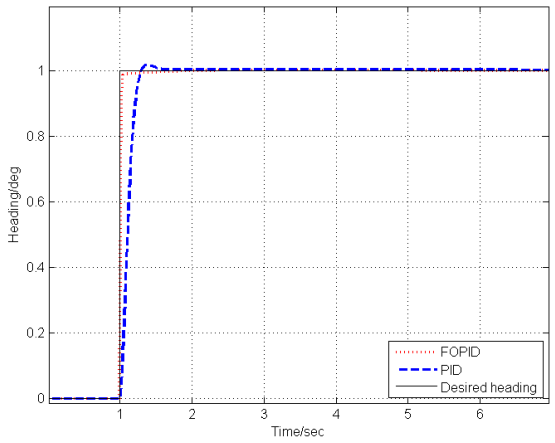

FIGURE 16. Comparison of step response of heading angle using FOPID and PID controllers.

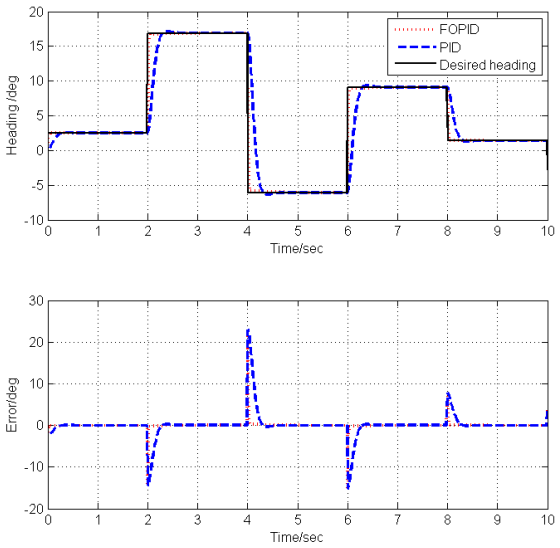

FIGURE 17. Comparison of white noise of heading angle using FOPID and PID controllers.

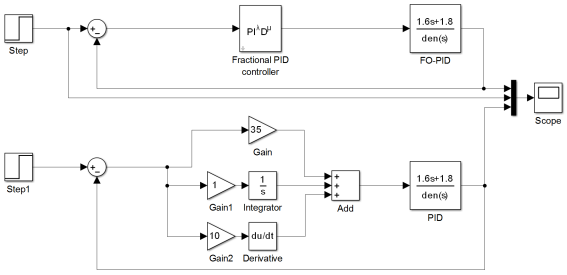

FIGURE 18. Simulink model of pitch angle for AUV using FOPID and PID controllers.

as shown in Fig.21. It is further demonstrated the better performance of fractional-order PID than traditional PID.

3) PARAMETERS OPTIMIZATION

The algorithms have been solved on a 3.20 GHz Intel(R) core(TM) i5-6500 desktop computer that has 16 GB of ram

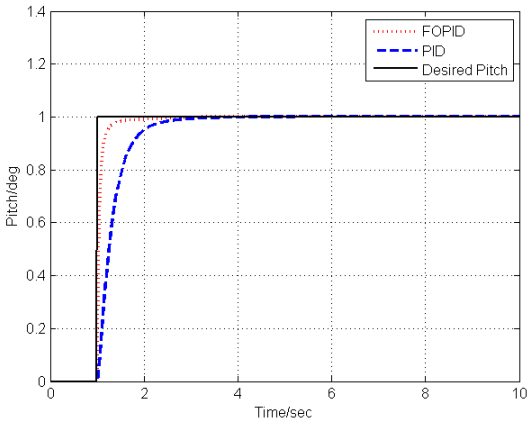

FIGURE 19. Comparison of step response of pitch angle using FOPID and PID controllers without overshoot.

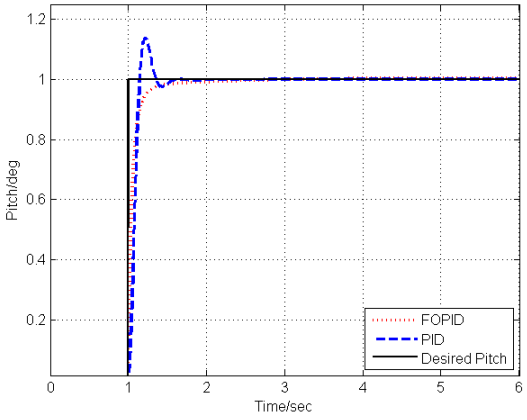

FIGURE 20. Comparison of step response of pitch angle using FOPID and PID controllers with the same rise-time.

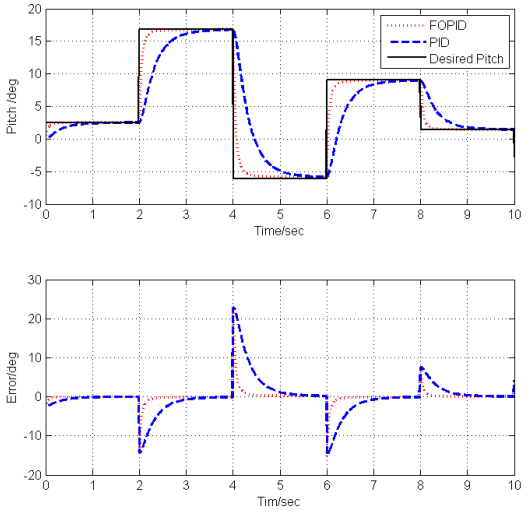

FIGURE 21. Comparison of white noise of pitch angle using FOPID and PID controllers.

and Microsoft Windows 7 operating system. Figure 22 and 23 provide the step response of heading and pitch angle using CQGA and GA, respectively. ITAE is adopted as objective

TABLE 3. Performance metric of simulation for pitch angle using FOPID and PID controllers.

Method	Settling time(s)	Over shoot(%)	SSE(m)
$FOPID_1$	2	0	0
PID_1	3	0	0
$FOPID_2$	2	0	0
PID_2	2	11.4	0

$FOPID_1$ and PID_1 denote step response without overshoot. $FOPID_2$ and PID_2 denote step response with the same settling time.

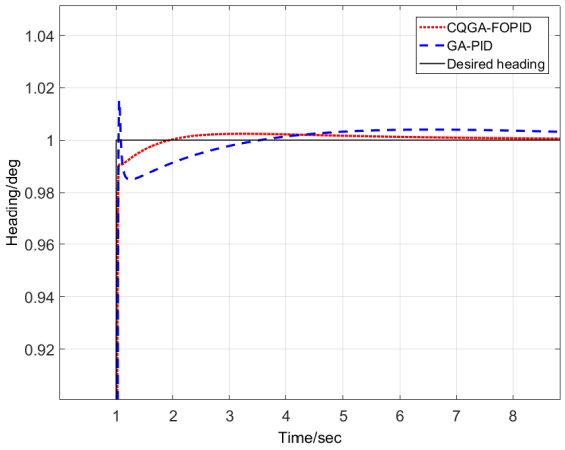

FIGURE 22. Comparison of the performance of heading angle using CQGA and GA

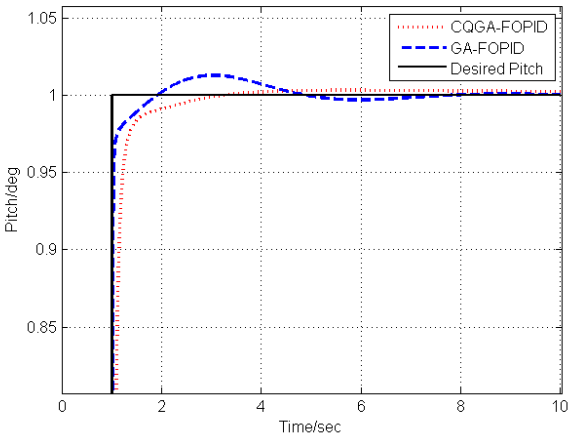

FIGURE 23. Comparison of the performance of pitch angle using CQGA and GA

function, as shown in (64). The results are summarized in Table 4. It is observed from Table 4, Fig.22 and Fig.23 that the heading angle controlled by the CQGA-FOPID controller exhibits smaller overshoot, shorter settling time and runtime, compared to GA-FOPID controller.

$$ITAE = \int_0^\infty t|e(t)|dt \tag{64}$$

B. EXPERIMENTS

The method proposed in this paper is validated on the *Sailfish* AUV independently developed at Underwater Vehicle Lab

TABLE 4. Performance metric of parameter optimization for heading and pitch with respect to CQGA and GA.

Method	Run time(s)	Settling time(s)	Over shoot(%)	K_p	K_i	K_d	λ	μ
$CQGA_1$	5.117	8	0.3	95	26	59	0.89	0.99
GA_1	75.165	12	1.5	28	10	59	0.87	0.88
$CQGA_2$	5.19	8	0	40	5	10	1.09	1.1
GA_2	87.638	8	1.3	90	99	57	1.14	1.07

$CQGA_1$and GA_1 denote parameter optimization for heading. $CQGA_2$ and GA_2 denote parameter optimization for pitch.

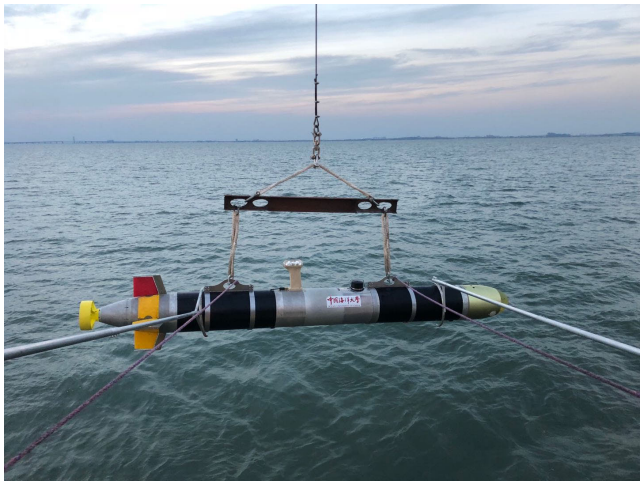

FIGURE 24. Photo of AUV *Sailfish*.

TABLE 5. Performance matrix of heading angle on sea trial using FOPID and PID controllers.

Method	Settling time(s)	Overshoot(%)	RMS(°)	RMSE(°)
FOPID	11	1.6	267.87	2.36
PID	11	2.5	266.16	4.31

of the Ocean University of China. *Sailfish* displacement is 260 Kg. It measures 3.8m in length, 32.4 cm in diameter and is equipped with several sensors(AHRS, Attitude and Heading Reference System; DVL, Doppler Velocity Log; GPS, Global Positioning System; SONAR, Sound Navigation and Ranging), as shown in Fig.24. The trial has been carried out on May 1, 2019 at NanJiang harbor, QingDao, in a sunny day, an air temperature of 18°C. The speed of south wind is 3-6 knots and the ocean waves are up to 0.1-0.5 m high.

1) HEADING

The comparison of PID and fractional-order PID control on trial is sketched in Table 5, Fig.25 and Fig.26. The desired heading angle is 270°, and the cruise speed is 1.0 m/s. Table 5 reports the overshoot, settling time, RMS (root mean square) and RMSE (root mean square error) of heading using these two controllers. It is apparent that the overshoot decreases 36% as well the steady-state error decreases 45%. The experiment further shows that the fractional-order PID controller has smaller steady-state error and overshoot.

2) DEPTH

The comparison of depth using fractional-order PID and PID controllers on trial is sketched in Table 6,

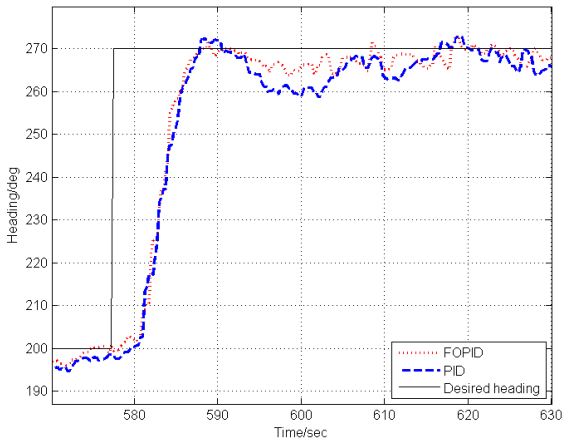

FIGURE 25. Comparison of the performance of heading angle using FOPID and PID controllers

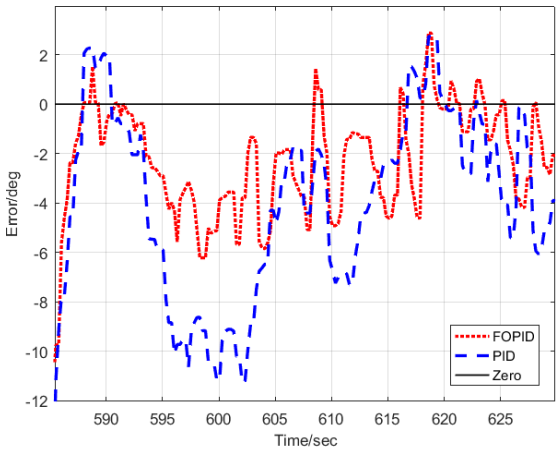

FIGURE 26. Comparison of the error of heading angle using FOPID and PID controllers

TABLE 6. Performance matrix of depth on trail using FOPID and PID controllers.

Method	Settling time(s)	Overshoot(%)	RMS(m)	RMSE(m)
FOPID	30	7.44	2.56	0.10
PID	40	17.28	2.62	0.18

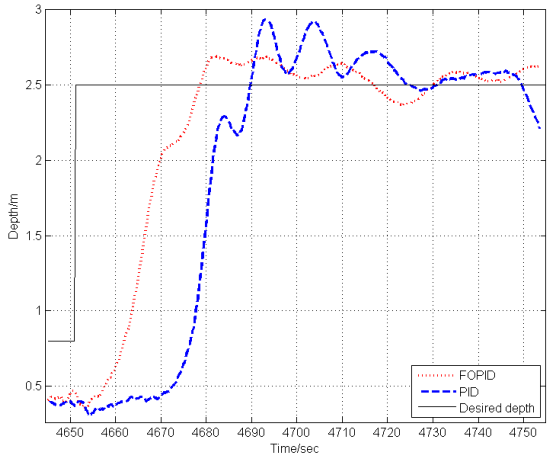

FIGURE 27. Comparison of the performance of depth using FOPID and PID controllers.

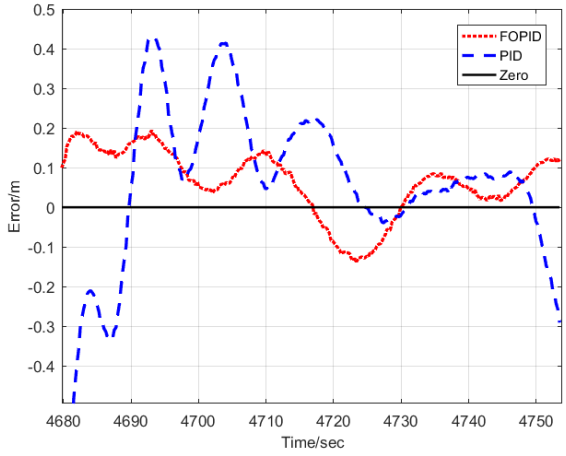

FIGURE 28. Comparison of the error of depth using FOPID and PID controllers.

TABLE 7. Performance matrix of path following for a circle using FOPID and PID controllers.

Method	Radius(m)	RMS(m)	RMSE(m)
FOPID	24	24.2922	0.4252
PID	24	24.7904	0.8728

Fig.27 and Fig.28. The desired depth is 2.5m, and the cruise speed is 1m/s. Table 6 reports the overshoot, settling time, RMS and RMSE of depth using these two controllers. The red dots indicate the depth employing fractional-order PID, the blue dashed line indicates the depth employing PID, and the black solid line indicates the desired depth. The fractional-order PID has shorter settling time and lower overshoot than PID. Obviously, it shows that the fractional-order PID improves the performance.

3) PATH FOLLOWING

The fractional-order PID controller is tested experimentally in two different scenarios. In the first scenario, the AUV follows the circle with the radius of 24m, and the cruise speed is 1m/s. The comparison using fractional-order PID and PID controllers on sea trial is presented in Fig.29 and Table 7. The red line with diamonds indicates the path following employing fractional-order PID, and the mean radius is 24.2922m. The blue line with stars indicates the path following employing PID, and the mean radius is 24.7904m. The black line indicates the desired path. The RMS errors are 0.4252m and 0.8728m, respectively. The fractional-order PID controller is validated to enhance the performance and attain the lesser overshoot.

Similarly, in the second scenario, the AUV follows the square with a side of length of 100m and the cruise speed is 1m/s. The comparison using fractional-order PID and PID

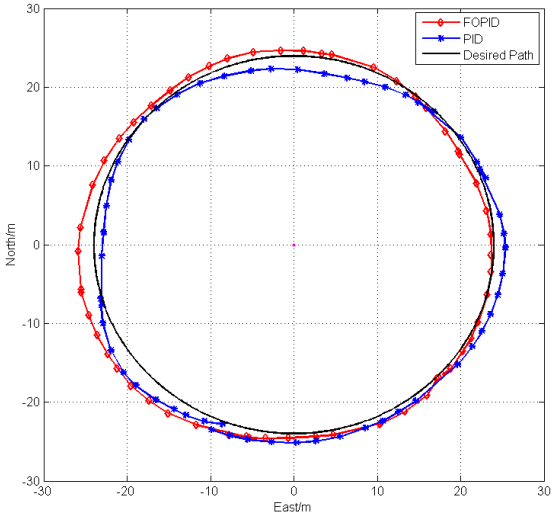

FIGURE 29. Scenario 1: Performance of path following of circles using FOPID and PID controllers.

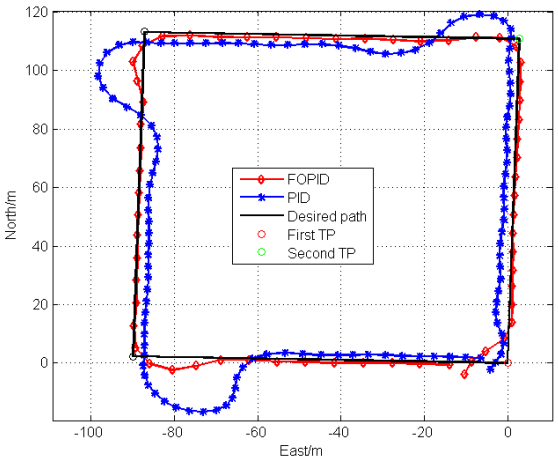

FIGURE 30. Scenario 2: Performance of path following of squares using FOPID and PID controllers.

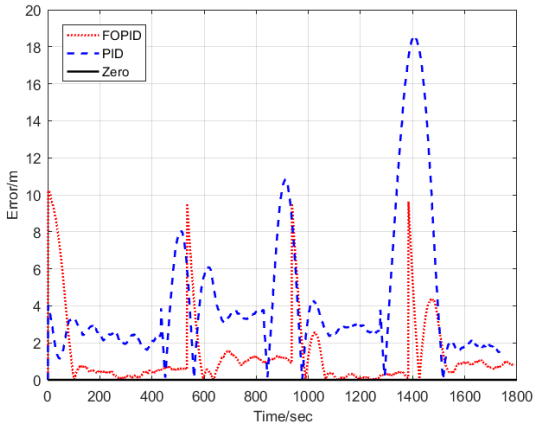

FIGURE 31. Scenario 2: Error of path following of squares using FOPID and PID controllers.

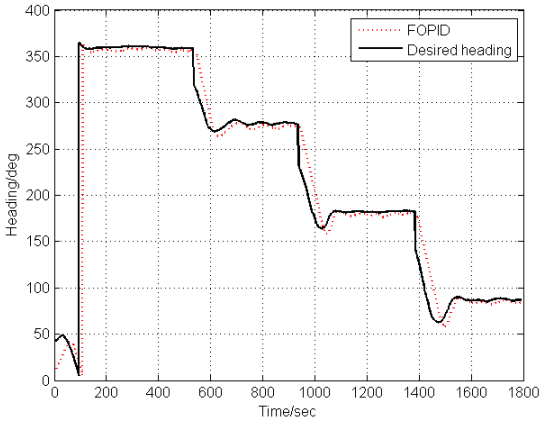

FIGURE 32. Comparison of the performance of heading angle using FOPID controller.

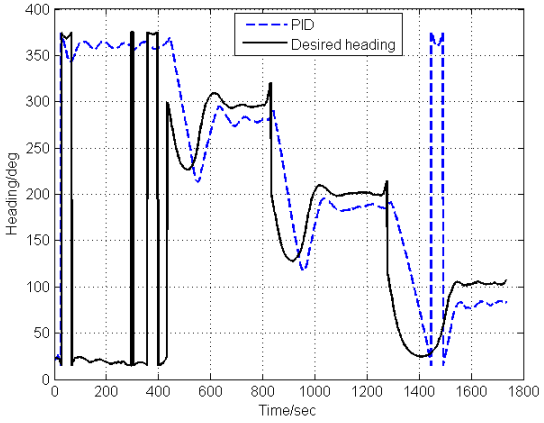

FIGURE 33. Comparison of the performance of heading angle using PID controller.

controllers on trial is presented in Fig.30 and Fig.31. The red line with diamonds indicates the path following employing fractional-order PID, and the blue line with stars indicates the path following employing PID. The black line indicates the desired path. The red circle is the first target point, and the green circle is the second target point. The RMS errors are 2.4307m and 5.7728m, respectively. The average relative errors are 0.6% and 1.4%, respectively. The error of PID controller is more than twice as much as the fractional-order PID controller.

When AUV moves along the desired path, the LOS (line-of-sight) method is performed to calculate the desired heading in real time. The desired heading is calculated according to the real-time position of AUV, its projection on the desired path and the lookahead distance. The comparisons of heading angles using fractional-order PID and PID controllers are illustrated in Fig.32 and Fig.33 respectively. The red rots indicate the measured heading via fractional-order PID and the black line indicates the desired heading computed by expected path. They are very close to each other. The blue dashed line indicates the measured heading via PID and the black line indicates the desired heading. Nevertheless, the deviation between the measured heading and the desired

heading is extremely large. Obviously, the performance of heading affects AUV reaching its desired path. It can clearly be seen that the performance of fractional-order PID controller is superior to PID.

V. CONCLUSION

In this paper, a fractional-order PID using cloud-model-based genetic algorithm is proposed. First, equations of motion in 6 freedoms of degree are established, which can be decoupled into longitudinal and lateral motions. The transfer functions of heading and pitch are deduced. The mathematical model is simulated with MATLAB program. Second, fractional-order PID controller has been designed for AUV, which is successfully used in heading control, diving control and path-following system on sea trial for the first time. The fractional-order closed-loop system has proven to be stable. By comparing simulations and experiments, the satisfactory performance, such as overshoot, settling time and steady-state error, has been achieved. Finally, a quantum genetic algorithm combining with cloud model theory is proposed, which is employed to tune parameters of fractional-order controller. Compared with GA, the performance of CQGA is tested by heading and pitch system. Owing to the randomness and stability tendency of cloud droplets, the crossover operator and mutation operator can be effectively improved to overcome the shortcomings of premature and slow searching speed. Numerical simulations show that CQGA avoids the pressure of selection, maintains the diversity of population in chromosome coding and effectively adjusts the parameters of the fractional-order PID controller.

In the future, CQGA will be carried out in practice, and various ocean conditions will be taken into consideration.

REFERENCES

[1] B. Jalving, "The NDRE-AUV flight control system," *IEEE J. Ocean. Eng.*, vol. 19, no. 4, pp. 497–501, Oct. 1994.
[2] M. H. Khodayari and S. Balochian, "Modeling and control of autonomous underwater vehicle (AUV) in heading and depth attitude via self-adaptive fuzzy PID controller," *J. Marine Sci. Technol.*, vol. 20, no. 3, pp. 559–578, 2015.
[3] T. Salgado-Jimenez, J.-M. Spiewak, P. Fraisse, and B. Jouvencel, "A robust control algorithm for AUV: Based on a high order sliding mode," in *Proc. MTS/IEEE Techno-Ocean*, Nov. 2004, pp. 276–281.
[4] R. Costa-Castelló, N. Carrero, S. Dormido, and E. Fossas, "Teaching, analyzing, designing and interactively simulating sliding mode control," *IEEE Access*, vol. 6, pp. 16783–16794, 2018.
[5] A. Nag, S. S. Patel, K. Kishore, and S. A. Akbar, "A robust H-infinity based depth control of an autonomous underwater vehicle," in *Proc. Int. Conf. Adv. Electron. Syst.*, Sep. 2013, pp. 68–73.
[6] A. M. Mashhad and S. K. M. Mashhadi, "H infinity robust controller comparison with PD like fuzzy logic controller for an AUV control," in *Proc. Iranian Joint Congr. Fuzzy Intell. Syst.*, Sep. 2016, pp. 1–5.
[7] C. Yu, X. Xiang, P. A. Wilson, and Q. Zhang, "Guidance-error-based robust fuzzy adaptive control for bottom following of a flight-style AUV with saturated actuator dynamics," *IEEE Trans. Cybern.*, to be published.
[8] R. Vilanova and A. Visioli, *PID Control in the Third Millennium*. London, U.K.: Springer, 2012.
[9] B. M. Vinagre, C. A. Monje, D. Xue, and Y. Chen, *Fractional-Order Systems and Controls: Fundamentals and Applications*. London, U.K.: Springer, 2010.
[10] I. Podlubny, "Fractional-order systems and $PI^{\lambda}D^{\mu}$ controllers," *IEEE Trans. Autom. Control*, vol. 44, no. 1, pp. 208–214, Jan. 1999.
[11] I. Podlubny, "Geometric and physical interpretation of fractional integration and fractional differentiation," *Fractional Calculus Appl. Anal.*, vol. 5, no. 4, pp. 230–237, 2001.
[12] D. B. Talange, S. D. Joshi, and S. Gaikwad, "Control of autonomous underwater vehicle using fractional order PI^{λ} controller," in *Proc. IEEE Int. Conf. Control Appl.*, Aug. 2013, pp. 1111–1116.
[13] S. D. Joshi and D. B. Talange, "Integer & fractional order PID controller for fractional order subsystems of AUV," in *Proc. IEEE Symp. Ind. Electron. Appl.*, Sep. 2013, pp. 21–26.
[14] S. D. Joshu and B. D. Talange, "Fractional order modeling and control of depth system of AUV a case study," in *Proc. 2nd Int. Conf. Adv. Comput. Sci. Eng. (CSE)*. Jul. 2013, pp. 157–161.
[15] M. S. Ajmal, M. Labeeb, and D. V. Dev, "Fractional order PID controller for depth control of autonomous underwater vehicle using frequency response shaping approach," in *Proc. Annu. Int. Conf. Emerg. Res. Areas, Magn., Mach. Drives*, Jul. 2014, pp. 1–6.
[16] N. Radmehr, H. Kharrati, and N. Bayati, "Optimized design of fractional-order PID controllers for autonomous underwater vehicle using genetic algorithm," in *Proc. Int. Conf. Elect. Electron. Eng.*, Nov. 2015, pp. 729–733.
[17] J.-Y. Cao, J. Liang, and B.-G. Cao, "Optimization of fractional order PID controllers based on genetic algorithms," in *Proc. Int. Conf. Mach. Learn. Cybern.*, Aug. 2005, pp. 5686–5689.
[18] R. V. Jain, M. V. Aware, and A. S. Junghare, "Tuning of fractional order PID controller using particle swarm optimization technique for DC motor speed control," in *Proc. IEEE 1st Int. Conf. Power Electron., Intell. Control Energy Syst. (ICPEICES)*, Jul. 2017, pp. 1–4.
[19] K. Oprzedkięwicz and K. Dziedzic, "A tuning of a fractional order PID controller with the use of particle swarm optimization method," in *Proc. Int. Conf. Artif. Intell. Soft Comput.*, 2017, pp. 394–407.
[20] C. Li, N. Zhang, X. Lai, J. Zhou, and Y. Xu, "Design of a fractional-order PID controller for a pumped storage unit using a gravitational search algorithm based on the Cauchy and Gaussian mutation," *Inf. Sci.*, vol. 396, pp. 162–181, Aug. 2017.
[21] X. Bo *et al.*, "A novel quantum—Inspired multi—Objective evolutionary algorithm based on cloud theory," *Automat. Panorama*, vol. 8, no. s2, pp. 145–150, 2011.
[22] A. Narayanan and M. Moore, "Quantum-inspired genetic algorithms," in *Proc. IEEE Int. Conf. Evol. Comput.*, May 1996, pp. 61–66.
[23] K.-H. Han and J.-H. Kim, "Genetic quantum algorithm and its application to combinatorial optimization problem," in *Proc. Congr. Evol. Comput.*, Jul. 2002, pp. 1354–1360.
[24] X. Zhu, J. Xiong, and J. Xiong, "Fault diagnosis of rotation machinery based on support vector machine optimized by quantum genetic algorithm," *IEEE Access*, vol. 6, pp. 33583–33588, 2018.
[25] D. Li, C. Liu, and W. Gan, "A new cognitive model: Cloud model," *Int. J. Intell. Syst.*, vol. 24, no. 3, pp. 357–375, Mar. 2009.
[26] G. Wang, C. Xu, and D. Li, "Generic normal cloud model," *Inf. Sci.*, vol. 280, pp. 1–15, Oct. 2014.
[27] M. Srinivas and L. M. Patnaik, "Adaptive probabilities of crossover and mutation in genetic algorithms," *IEEE Trans. Syst., Man, Cybern.*, vol. 24, no. 4, pp. 656–667, Apr. 1994.
[28] C. H. Dai, Y. F. Zhu, and W. R. Chen, "Adaptive probabilities of crossover and mutation in genetic algorithms based on cloud model," in *Proc. IEEE Inf. Theory Workshop (ITW)*, Punta del Este, Uruguay, Oct. 2006, pp. 710–713.
[29] L. McCue, "Handbook of marine craft hydrodynamics and motion control," *IEEE Control Syst. Mag.*, vol. 36, no. 1, pp. 78–79, Feb. 2016.
[30] T. Prestero, "Development of a six-degree of freedom simulation model for the REMUS autonomous underwater vehicle," in *Proc. IEEE OCEANS*, Nov. 2002, pp. 450–455.
[31] J. Wan, B. He, Y. Shen, W. Liu, X. Ding, and S. Gao, "Heading multi-mode control based on soft-switching for autonomous underwater vehicle," *Ocean Eng.*, vol. 164, pp. 672–682, Sep. 2018.
[32] J. Hu, H. Kawamura, H. Hong, and Y. Qi, "A review on the currents in the South China Sea: Seasonal circulation, South China Sea warm current and Kuroshio intrusion, " *J. Oceanogr.*, vol. 56, no. 6, pp. 607–624, 2000.
[33] D. Matignon, "Stability properties for generalized fractional differential systems," in *Proc. ESAIM*, vol. 5, no. 5, pp. 145–158, 1998.
[34] Y. Yang, R. Liu, Y. Chen, T. Li, and Y. Tang, "Normal cloud model-based algorithm for multi-attribute trusted cloud service selection," *IEEE Access*, vol. 6, pp. 37644–37652, 2018.

[35] T. Aleksei, P. Eduard, and B. Juri, "A flexible MATLAB tool for optimal fractional-order PID controller design subject to specifications," in *Proc. Chin. Control Conf.*, Jul. 2012, pp. 4698–4703.
[36] A. Tepljakov, E. Petlenkov, and J. Belikov, "FOMCON: Fractional-order modeling and control toolbox for MATLAB," in *Proc. 18th Int. Conf. Mixed Design Integr. Circuits Syst. (MIXDES)*, Jun. 2011, pp. 684–689.
[37] A. Tepljakov, "FOMCON: Fractional-order modeling and control toolbox," in *Fractional-Order Modeling and Control of Dynamic Systems*. Cham, Switzerland: Springer, 2017, ch. 6, pp. 107–129. doi: 10.1007/978-3-319-52950-9_6.
[38] A. Oustaloup, F. Levron, B. Mathieu, and F. M. Nanot, "Frequency-band complex noninteger differentiator: Characterization and synthesis," *IEEE Trans. Circuits Syst. I, Fundam. Theory Appl.*, vol. 47, no. 1, pp. 25–39, Jan. 2000.

JUNHE WAN was born in Yichun, Heilongjiang, China, in 1982. She received the B.S. degree in technique and instrumentation of measurements and the M.S. degree in measuring and testing techniques and automation from Liaoning Shihua University, China, in 2004 and 2006, respectively. She is currently pursuing the Ph.D. degree in intelligent information and communication systems with the Ocean University of China, Qingdao, China. She has published one journal article and applied one China invention patent. Her research interest includes motion control based on soft-switching and threshold-switching and optimization algorithm for AUV.

BO HE (M'01) was born in Qingdao, Shandong, China, in 1971. He received the M.S. and Ph.D. degrees from the Harbin Institute of Technology, China, in 1996 and 1999, respectively. From 2000 to 2003, he was a Postdoctoral Fellow with Nanyang Technological University, Singapore, where he worked on mobile robots, unmanned vehicles, and research works included precise navigation, control, and communication. In 2004, he joined the Ocean Univercity of China (OUC), where he is currently a Full Professor and the Deputy Head of the Department of Electronics Engineering, College of Information Science and Engineering. His current research interests include AUV design and applications, AUV SLAM, AUV control, and machine learning.

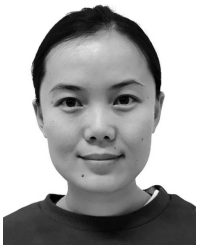

DIANRUI WANG was born in Rizhao, Shandong, China, in 1990. She received the B.S. degree in communication engineering from Qingdao Agricultural University, Qingdao, China, in 2014. She is currently pursuing the Ph.D. degree in intelligent information and communication systems with the Ocean University of China, Qingdao, China. She has published three conference papers. She was a recipient of the Excellent Poster Award for the IEEE-OES/2017 Underwater Technology.

TIANHONG YAN received the B.S. degree in mechanical engineering from Liaoning Technical University, Liaoning, China, in 1993, the M.S. degree in mechanical engineering from the Xi'an University of Technology, Shaanxi, China, in 1996, and the Ph.D. degree in aerospace engineering and mechanics from the Harbin Institute of Technology, Harbin, China, in 1999. He has been a Full Professor with China Jiliang University, since 2009. His current research interests include integrated system design, mechatronics systems, motion control, and electronics packaging equipments.

YUE SHEN, photograph and biography not available at the time of publication.